Northward channel flow in northern Tibet revealed from 3D magnetotelluric modelling

Wenbo Wei [a], Florian Le Pape [b,*], Alan G. Jones [b], Jan Vozar [b], Hao Dong [a], Martyn J. Unsworth [c], Sheng Jin [a], Gaofeng Ye [a], Jianen Jing [a], Letian Zhang [a], Chengliang Xie [a]

[a] China University of Geosciences Beijing, 29 Xueyuan Road, Beijing 100083, China
[b] Dublin Institute for Advanced Studies, 5 Merrion Square, Dublin 2, Ireland
[c] Department of Physics, University of Alberta, Edmonton, AB T6G 2J1, Canada

ARTICLE INFO

ABSTRACT

The Kunlun fault defines one of the major northern tectonic boundaries of the Tibetan plateau. Previous geophysical studies have detected a major change in rheology across this boundary, but it is not clear how this is related to models that have invoked crustal flow. The lithospheric resistivity structure of the Kunlun fault has been investigated by both the INDEPTH III and IV magnetotelluric (MT) transects. All the MT data were processed using modern statistically-robust methods, and have been analysed for directionality and dimensionality. In order to improve understanding of the anisotropic distribution of melt previously revealed by our remodelling of the INDEPTH III MT data, a variant approach on 3D inversion of 2D profiles was investigated to explore and improve lateral resolution. In addition to the apparent surficial deformation associated with the sinistral strike-slip Kunlun fault, the 3D modelling of the INDEPTH MT data reveals that complex deformation processes are occurring at mid-crustal depths in northern Tibet. The 3D MT inversion results, supported by synthetic modelling, particularly confirm and highlight the presence of separate north–south intrusions of conductive material crossing the Kunlun fault into the more resistive Kunlun–Qaidam block. These north–south intrusions are interpreted to be associated with the horizontal channel flow of partially molten Songpan–Ganzi crust into two (or more) separated channels moving northwards and crossing the surficial trace of the Kunlun fault at mid-to-lower crustal depths.

© 2014 Elsevier B.V. All rights reserved.

1. Introduction

The first INDEPTH (InterNational DEep Profiling of Tibet and the Himalaya) experiments in the early to mid-1990s collected seismic and magnetotelluric data that revealed the presence of a partially molten middle crust beneath southern Tibet (Nelson et al., 1996, and papers in that special issue). The revolutionary interpretation of those data by Nelson et al. (1996) instigated a whole new insight into crustal processes during continent–continent collision and has led to geodynamicists, geologists and tectonicists examining the concept of "channel flow". The Himalayan channel flow model (e.g., Beaumont et al., 2001) was directly built from those results in order to explain the high-grade metamorphic rocks, leucogranites and migmatites exposed in the Greater Himalayan sequence (Godin et al., 2006), with the INDEPTH-II 1995 magnetotelluric results being key to the development of the observation of partial melt in the crust (Chen et al., 1996).

Furthermore, in order to account for the overall deformation observed in the whole of the Tibetan Plateau, a range of geodynamic models have been proposed, the most popular of them being the crustal flow model of Royden (Royden et al., 1997; Clark and Royden, 2000). This type of deformation is dominated by rapid ductile flow in the middle and/or lower crust (e.g., Klemperer, 2006). The crustal flow has been proposed to escape to the east, moving around the eastern Himalayan syntaxis and being blocked by the rigid Sichuan basin (Clark and Royden, 2000). However, in contrast to the observations along the Himalaya, there is no direct geological evidence for crustal flow beneath the eastern margin of the Tibetan Plateau, as the Longmenshan ranges do not show either horizontal extrusion of deep crustal metamorphic rocks or equivalents to the Main Central thrust (MCT) or South Tibetan detachment (STD) (Searle et al., 2011). Harris (2007) proposed that "channel tunnelling" (Beaumont et al., 2001) could be occurring in eastern Tibet, as the weak crustal layer may not reach the surface. Medvedev and Beaumont (2006) suggested the channel flow model as a

---

* Corresponding author.

mechanism to characterize the progressive growth of the Tibetan plateau.

In central Tibet, the absence of seismic evidence for earlier accretion in the deep crust has been related to lateral escape by ductile flow (Haines et al., 2003). This observation was also recently supported by the widespread low velocities in the middle-to-lower crust of northern Tibet imaged from ambient-noise tomography (Karplus et al., 2013). Magnetotelluric (MT) studies have significantly contributed to the characterization of the Tibetan crustal flow (Chen et al., 1996; Li et al., 2003; Unsworth et al., 2004; Rippe and Unsworth, 2010; Bai et al., 2010; Le Pape et al., 2012). MT studies highlighted the presence of two laterally-extensive mid-crustal conductors that were interpreted as channels of crustal flow or shear zones on the margins of a region of extruding crust extending from the Tibetan plateau into southwest China and covering a horizontal distance of more than 800 km (Bai et al., 2010). Low shear-wave velocities imaged from surface-wave tomography in southeastern Tibet show spatial variations in the strength of the middle and lower crust (Yao et al., 2008). Thus, Bai et al. (2010) and Yao et al. (2008) are in agreement that the inferred crustal flow in Tibet may characterize a pattern of deformation more complex than the previously established model of Clark and Royden (2000).

INDEPTH Phase IV was initiated with its overarching goal to develop a better understanding of the structure and evolution of the northern margins of the Tibetan plateau defined by the Kunlun and Altyn Tagh faults. In particular, seismic results from INDEPTH IV have highlighted the possible flow of the weaker and more easily deformable Songpan–Ganzi crust into the crust beneath the Qaidam basin (Karplus et al., 2011; Mechie et al., 2012). This interpretation is also supported by the 2D anisotropic re-modelling of the INDEPTH III MT data that inferred that partial melt was intruding across the Kunlun fault in a finger-like manner (Le Pape et al., 2012). However, the study of Le Pape et al. (2012) was not able to establish definite constraints on the geometries of the melt intrusions. In order to investigate further the pattern of melt distribution within the crust beneath the Kunlun fault, the new MT data from the INDEPTH phase IV campaign was combined with the northernmost stations of the INDEPTH III 600-line profile, previously interpreted by Unsworth et al. (2004) and Le Pape et al. (2012), to obtain a 3D resistivity model of the Kunlun region. Due to the limitations of station coverage, the array was not ideal for a 3D inversion. Thus a novel approach was developed for the 3D inversion of MT data located on 2D profiles. This investigated ways to improve the lateral resolution by limiting the introduction of off-profile artefacts.

2. Geological setting

2.1. Songpan–Ganzi terrane

The Songpan–Ganzi terrane is bounded to the north by the Kunlun fault (KF), a reactivation of the older Anyimaqen–Kunlun–Muztagh suture that separates the terrane from the Kunlun–Qaidam block (Fig. 1). To the south, the Songpan–Ganzi terrane is separated from the Qiangtang terrane by the Jinsha suture (JRS, Fig. 1). The terrane consists mostly of Upper Triassic marine strata characterized by a thick sequence of turbidites, also named the Songpan–Ganzi flysch complex, that are several kilometres in thickness lying on top of Palaeozoic marine sediments belonging to the passive margin of north China (Yin and Harrison, 2000; Gehrels et al., 2011). The Songpan–Ganzi flysch complex underwent intense folding and thrusting during the Triassic collision between the North and South China blocks (Burchfiel et al., 1995; Yin and Nie, 1996), forming the

Anyimaqen–Kunlun–Muztagh suture. East of the Lhasa–Golmud highway in the north of the terrane, the Bayan Har Shan defines the southern branch of the Kunlun Shan. The Bayan Har mountains are characterized by poorly dated low-grade slate belts, which include Triassic sedimentary rocks and Mesozoic plutonic intrusions (Cowgill et al., 2003; Huang et al., 2004).

2.2. Kunlun–Qaidam terrane

The Eastern Kunlun–Qaidam Terrane lies between the Anyimaqen–Kunlun–Muztagh suture to the south and the Qilian suture to the north (Yin and Harrison, 2000). The terrane is bounded in the south by the Kunlun mountains, or Kunlun Shan, along the active sinistral Kunlun fault. Near the Lhasa–Golmud highway (Fig. 1), the fault splits in two branches, characterizing the Kunlun fault (KF) and the South Kunlun fault (SKF) (Fig. 1). Different interpretations have been offered concerning the structure of the Kunlun fault at depth. Kirby et al. (2007) proposed that it terminates within the thickened crust of the Tibetan plateau, whereas Meyer et al. (1998) suggested the fault to be a lithospheric discontinuity that extends as deep as 150 km (Tapponnier et al., 2001). More recently, the seismic results of Karplus et al. (2011, 2013) indicated that the fault may not extend deeper than 30 km, i.e., the middle of the overly-thickened Tibetan crust. The Kunlun fault is likely to be coeval with the Miocene extension and links the eastward expansion of the Tibetan plateau with the north–south trending extensional systems (Yin and Harrison, 2000). The Kunlun Shan exhibit mainly Paleozoic and lower Mesozoic rocks intruded by early Paleozoic and Permo-Triassic arc-type magmatism, characterized as the Kunlun batholith (Yin and Harrison, 2000). The Qaidam basin is bounded by the Kunlun Shan in the south, the Altan Shan in the northwest and the Qilian Shan-Nan Shan in the northeast (Fig. 1 inset). As fold and thrust belts developed along the foreland of the Kunlun Shan mountain belt, the Qaidam basin expanded progressively toward the north and east (Yin et al., 2008). The southeast-dipping North Kunlun thrust (NKT) appends Proterozoic metamorphic rocks and Paleozoic sedimentary and igneous rocks over the Tertiary and Cenozoic strata of the Qaidam crust (Yin and Harrison, 2000).

3. MT data analysis

The INDEPTH IV MT data were acquired between late Spring and early Summer 2010 and define the 6000 profile. Originally, it was planned for them to be acquired in 2009, but the very low sunspot activity at the tail of Solar Cycle 23 precluded acquisition. As depicted on Fig. 1, the new MT 6000 profile (sites denoted by purple squares) is located to the east of the previously collected INDEPTH III 600-line (sites denoted by black squares) and extends from the middle of the Songpan–Ganzi terrane, in the western Bayan Har Shan, to the southern edge of the Qaidam basin. The INDEPTH III 600 and INDEPTH IV 6000 profiles become closely aligned in the Qaidam basin as they meet up south of the North Kunlun thrust (NKT) on the only road crossing the Kunlun range (Fig. 1). The new 6000 MT transect was also purposely collocated with the INDEPTH IV seismic profile (Karplus et al., 2011; Mechie et al., 2012).

For this 3D study, MT data from a total of 38 sites from both INDEPTH III and IV transects were selected, mainly from the Kunlun fault area (Fig. 1). The data include 14 sites from the INDEPTH III 600-line and 24 sites from the new INDEPTH IV 6000-line. Overall, the data comprise 10 long period MT (LMT) sites merged with broadband (BBMT) data sites from each profile, the remaining 18 sites only having BBMT data. For the INDEPTH IV sites, all the LMT data were processed using the processing method
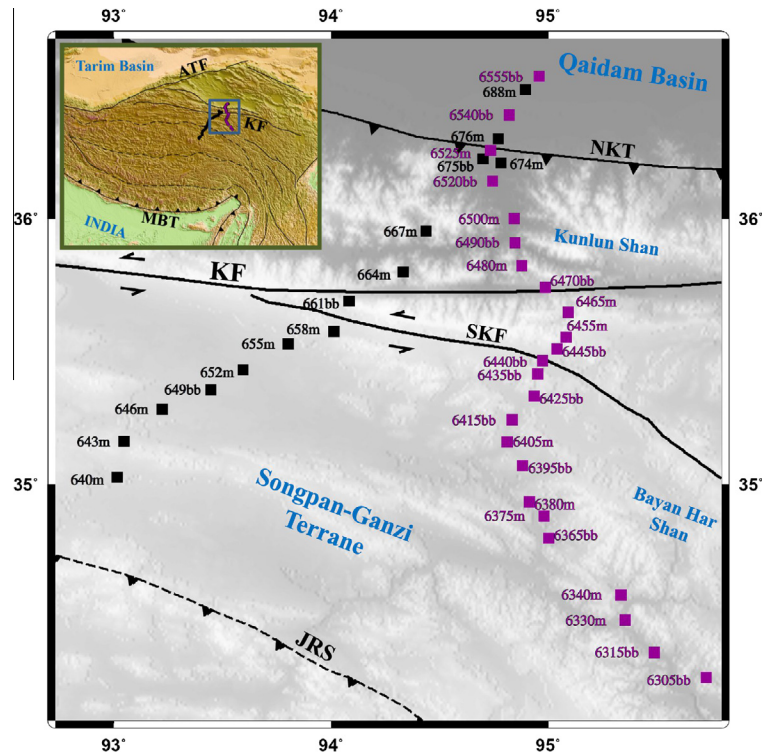
Fig. 1. Sites location for the MT data used in the 3D inversion. The data used combine selected sites from both INDEPTH III (black) and IV (purple) profiles. ATF, Altyn Tagh fault; KF, Kunlun fault; MBT, Main Boundary thrust; JRS, Jinsha River suture; SKF, South Kunlun fault; NKT, North Kunlun thrust. (For interpretation of the references to colour in this figure legend, the reader is referred to the web version of this article.)

of Smirnov (2003). The BBMT data were processed using the commercial code from Phoenix Geophysics which is based on the algorithm of Jones and Jödicke (1984, method 6 in Jones et al., 1989), which uses a method called in the statistical literature Least Trimmed Squares developed independently at the same time as Jones and Jödicke (1984) by Rousseeuw (1984). Both the LMT and the BBMT data were processed using remote reference data to reduce the effects of noise contributions on the MT impedance tensor estimates. As mentioned in Le Pape et al. (2012), the INDEPTH III time series data were processed with the codes from Egbert (1997) and Jones et al. (1989) using remote reference data when available. For both INDEPTH III and IV, the BBMT and LMT data were merged at common locations.

Prior to inversion, the dimensionality of the data and the distribution of regional conductive structures were investigated qualitatively through phase tensor and induction vector analysis for different period bands (Fig. 2). The main advantage of these tools is that they are independent of the electric effects of galvanic distortion (but not the magnetic effects) (Jones, 2012). The real induction arrows are plotted in the Parkinson's convention (Parkinson, 1959), meaning that they are reversed so that they will point towards conductive anomalies (Jones, 1986) (in contrast to the Weise convention, where the arrows points away from conductors). Not all sites showed good quality tipper data, therefore only induction arrows from selected sites have been introduced on Fig. 2. The phase tensor ellipses are plotted with the skew angle. The skew angle measures the asymmetry in the MT response and therefore large values of skew angle can be linked to the presence of 3D regional conductive structures (Caldwell et al., 2004). With values outside the [−3° 3°] interval, it can be considered that the data is exceeding the limits of quasi 2D approximations. Furthermore, the direction of the phase tensor major axis will usually align with the direction of the maximum inductive current flow (Caldwell et al., 2004). However, since the induction arrows

and phase tensor do not sample the same volume they cannot be always comparable. Only period longer than 100 s were investigated to focus mainly on the regional structures but also because at the shorter periods the induction vectors were relatively scattered. On Fig. 2, both phase tensor and induction vector parameters have been averaged to an error-weighted mean over each period interval. Over most period intervals, both phase tensor ellipses and induction vectors calculated from the INDEPTH data show a strong consistency between neighbouring sites and periods.

To the north, the effects of the high conductivity of the Qaidam basin, that is related to extensive salt deposits (Kezao and Bowler, 1986), are seen on the northern most stations. The induction vectors sense the high conductivity basin by pointing to the north, at periods <800 s. It is also worth noting that the low resistivity layer in the Qaidam Basin limits the depth of penetration of the MT signals, due to the strong screening effects of the conducting layer. At most sites located south of the SKF, there is an overall east–west trend in the orientation of the ellipses, in agreement with the directions of the main geological sutures in the study area. Between the SKF and the NKT, the real induction vectors, although not strong, point west, indicating a region of more complex 3D structure. This 3D signature is confirmed by the high skew values observed in the Kunlun area. Those high values are likely associated with small- to middle-scale 3D structures located beneath the Kunlun mountains.

4. 3D modelling of MT data from northern Tibet

In this section we present the 3D inversion models derived from the INDEPTH III and IV MT data in association with a 3D inversion of synthetic MT data that explored the limitations in lateral resolution caused by the restricted grid of MT stations. The algorithm used for the 3D inversions was WSINV3DMT, which is based on
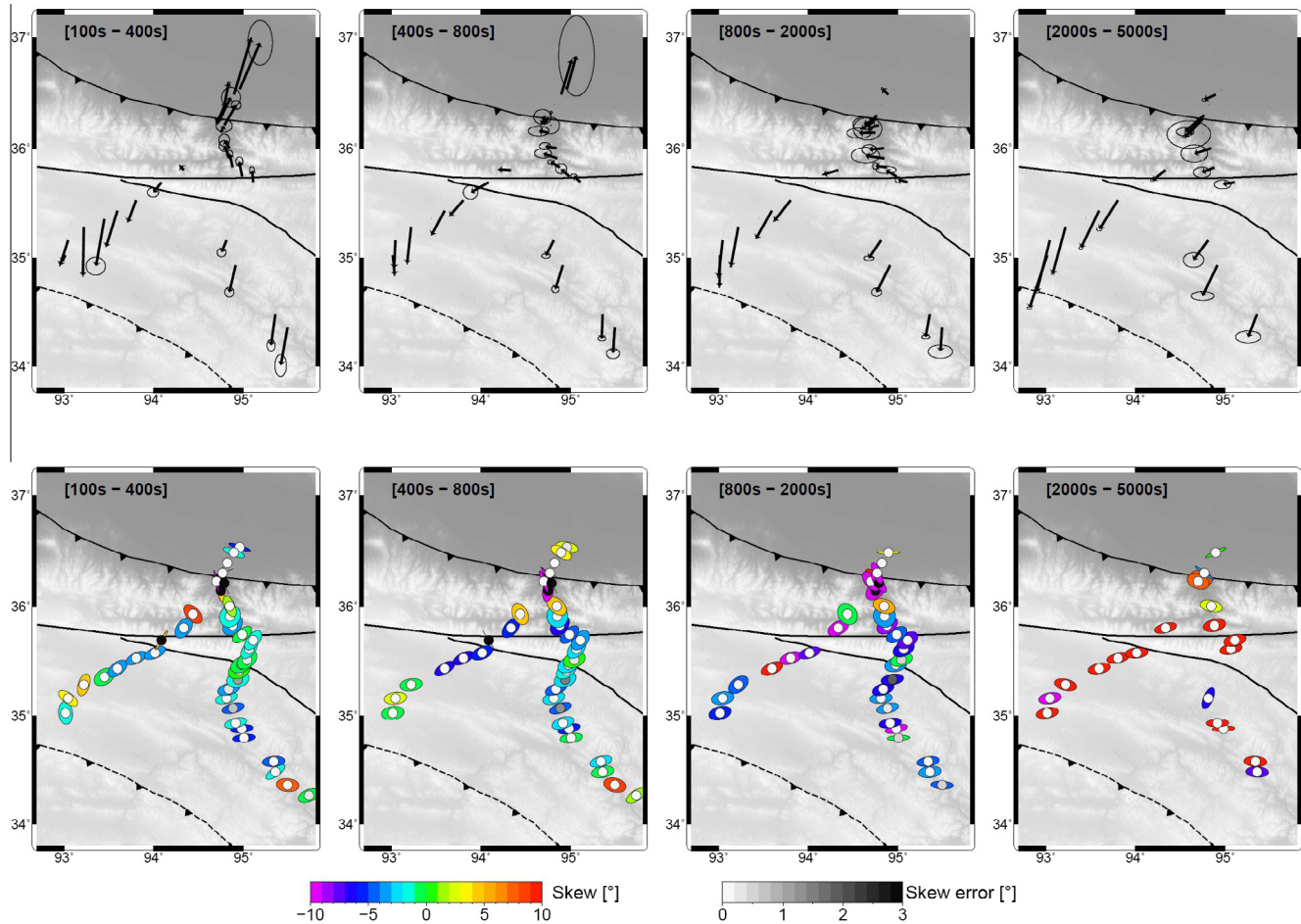
Fig. 2. Induction arrows (top - only selected sites) and phase tensor ellipses (bottom) for the INDEPTH sites plotted for different period intervals. The real induction arrows are plotted under Parkinson's convention. The errors on the induction vectors are plotted as ellipses that indicate the deviation from each component of the induction vectors. The phase tensor ellipses are normalized by their major axes and filled with the *skew angle*. The phase tensor ellipses are plotted so that the horizontal axis corresponds to an east–west orientation. The errors on the skew angle are plotted on top of each phase tensor ellipses.

data space inversion method and developed from the OCCAM minimum-norm approach (Siripunvaraporn et al., 2005a). Furthermore, it is worth noting that, due to the sparse stations layout, 3D inversion applied on 2D profiles should include all elements of the impedance tensor to improve off-profile resolution of nearby structures, as highlighted in Siripunvaraporn et al. (2005b) and Kiyan et al. (2013). Therefore, in the following 3D inversions of real and synthetic MT data, the full impedance tensor responses were inverted. In this study the objective was to primarily focus on the comparison in lateral resolution from different approaches of 3D modelling of both real and synthetic data impedances. For this reason and due to the poor quality of the tipper data for a few sites, no tipper data were introduced in the modelling. For each model, the misfit was reduced by running a few successive inversions using each resulting model as the starting and *a priori* model for the next inversions. The size of the 3D mesh used for the inversion of INDEPTH data was $80 \times 75 \times 44$ cells with a 5×5 km horizontal gridding in a square zone defined by the stations locations. For the synthetic modelling, the size of the 3D mesh used was $60 \times 61 \times 48$ cells with also a 5×5 km horizontal gridding around the stations.

4.1. 3D inversion of the INDEPTH III and IV data

The starting model and *a priori* model for the initial inversion was a 100 Ω m layer located above a fixed 10 Ω m halfspace (i.e.,

locked during inversion) at 410 km that represented the mantle transition zone. This deep basal conductor is required in all 2D and 3D modelling of MT data to ensure that the boundary condition on the base of the model is satisfied and to prevent bleeding down of features as a consequence of the spatial regularization. An error floor of 5% of the geometrically-averaged off-diagonal impedances was used to set a minimum error bar of $0.05 * (Zxy * Zyx)^2$ applied on all four elements of the impedance tensor during the inversion. Periods in the range 0.003–10,000 s were used and uniformly distributed with 4 periods per decade. The final 3D inversion model is plotted in Fig. 3 as several horizontal slices and vertical cross-sections. The 3D inversion of the 38 MT sites selected from both INDEPTH III and IV profiles, gave an overall RMS (Root Mean Square) misfit of 2.3. Furthermore, the misfit at each site describes a relatively homogeneous error partitioning across each station, although two sites in the Kunlun Shan area show high RMS misfit values (Fig. 3). As seen in Fig. 4, the overall observed and calculated responses are very similar, except for some localized exceptions. For instance, one of the most striking differences between the observed and calculated data occurs at the shortest periods of INDEPTH IV data in the XX and YY components. For those components, both the apparent resistivity and phase exhibit 3D signatures in the observed responses whereas the calculated responses appear more 1D. This difference is mainly due to the size of the mesh used in the inversion, which was limited by computational restrictions.
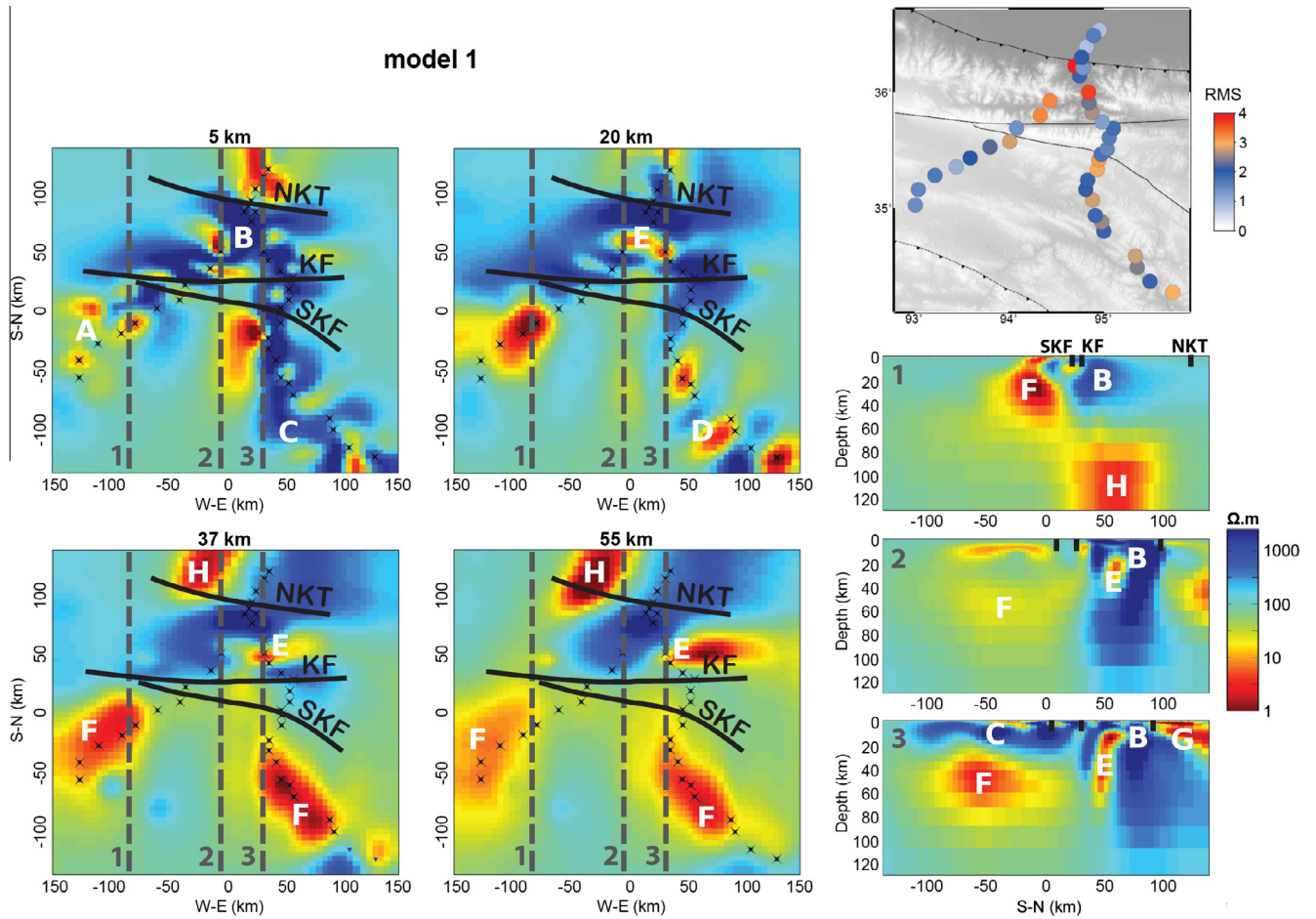
Fig. 3. 3D model 1 of the INDEPTH data obtained from the inversion of the full impedance tensor. The 3D model is plotted for several horizontal slices at different depths and for cross-sections with locations shown on plane views. The RMS misfit of the inversion is shown for each site on the top right corner. KF, Kunlun fault; SKF, South Kunlun fault; NKT, North Kunlun thrust.

Shallower crustal features can be clearly seen on the horizontal slice at 5 km. The trace of the NKT is unmistakably highlighted by the transition between the more resistive terrane of the Kunlun ranges and the more conductive sediments of the Qaidam basin to the north. The traces of both the KF and the SKF are also quite coherent with the surrounding resistivity distribution, particularly at the level of the 600-line. To the south, conductive structure "A" following the 600-line profile is electrical evidence of the sediments of the Songpan–Ganzi terrane, including the widespread Triassic flysch deposits. Finally, the main resistive features observed at 5 km depth on the 3D model correlate relatively well with the resistive crust "B" of the Kunlun Shan in the north and the resistive crust "C" of the western Bayan Har mountains to the east at the southern end of the INDEPTH IV profile (Fig. 3). Down to 20 km, the plan view shows a widespread conductive anomaly to the south of the INDEPTH III profile, whereas south of the INDEPTH IV line there is a strong alternation between conductive and resistive structures "D", likely related to the more complex crustal structure of the Bayan Har mountains. Further north, the resistive root "B" of the Kunlun mountains can also be seen, but a conductive anomaly "E" is located where both profiles meet between the surficial traces of the KF and the NKT. When reaching the 37 and 55 km depth views of the 3D model, the 600 and 6000 lines show a significant conductive anomaly "F" south of the SKF. Although less conductive, the anomaly "F" extends further north across the KF. Meanwhile, the conductive feature "E" observed at 20 km south of the NKT migrates further east of the 6000 line.

Both cross-sections, labelled 2 and 3 in Fig. 3, show that the mid-crustal conductor "F" located beneath the Songpan–Ganzi terrane weakens further to the north as it extends beneath the Kunlun fault system (Fig. 3). Furthermore, on a more global scale they also reveal the clear separation between the Tibetan conductive crust to the south and a more resistive lithosphere to the north beneath the Kunlun–Qaidam block. A smeared conductive layer "G" characterizing the Qaidam basin can also be seen on cross section 3. Although mainly located outside of the profile and therefore poorly constrained, cross-section 1 (Fig. 3) was chosen to highlight the presence of the conductive structure "H" located in the upper mantle north of the Kunlun fault. This conductive anomaly can also be seen on the 37 and 55 km plan views as well as at the northern edge of cross-section 2 as it becomes shallower towards the east. This anomaly "H" is likely to be an inversion artefact that reflects the lack of lateral resolution in the inversion, due to the paucity of data controlling it, and therefore must be treated with caution.

These inversion results, although 3D, are derived from two relatively linear profiles which raises questions about the limits of lateral resolution and the spreading of anomalies as an artefact of the smoothness regularization. In order to test for resolution and obtain a better understanding of the limits of a one-profile 3D inversion, some of the 3D synthetic models for northern Tibet, already discussed in Le Pape et al. (2012) are re-considered for the 3D inversion of a synthetic profile below.
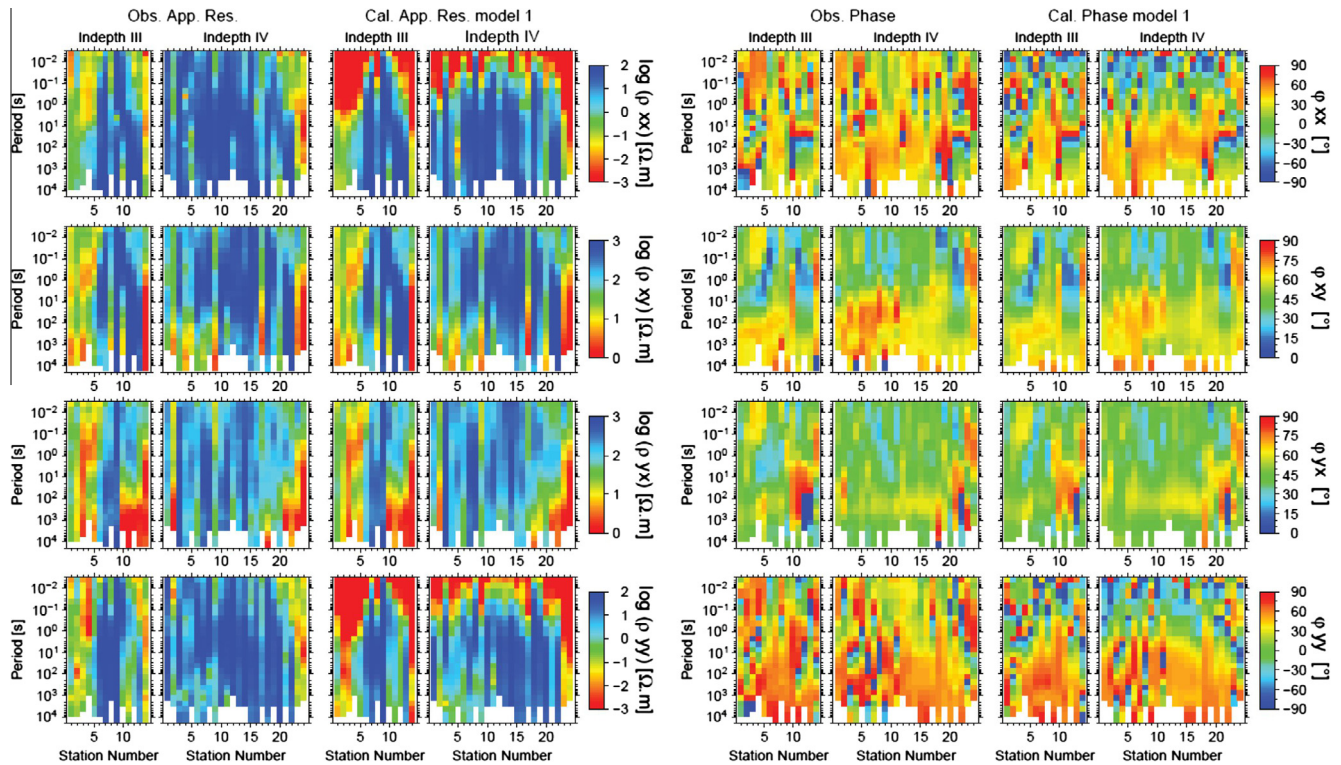
Fig. 4. Observed and calculated data from the inversion model 1. The data is separated as INDEPTH III and IV sections. For each section, the station numbers increase to the north. The data is plotted as pseudo-sections of apparent resistivity and phase for all 4 components of the impedance tensor.

4.2. Synthetic modelling and inversions

Although the inversion model presented above is fully 3D, it must be appreciated that it is mainly the result of the inversion of MT data on two sub-parallel profiles. The apparent lack of station coverage, in contrast to an ideal layout of stations in a grid manner, raises questions about the limit of lateral resolution in the 3D model. However, as presented by Siripunvaraporn et al. (2005b), 3D inversion of a 2D profile can significantly improve the interpretation of structures located underneath and, significantly, around the profile. Here, two particular models A and B, shown in Fig. 5, were investigated for 3D resolution. For consistency, they are based on the 3D synthetic models already presented in Le Pape et al. (2012). Both models were generated to account for melt intrusions defining the 3D resistivity transition between the Songpan–Ganzi and the more resistive eastern Kunlun–Qaidam block to the north observed in the recent 2D anisotropic MT model of the 600-line. The models describe similar geometries and only differ through the orientation of the intrusions. This synthetic study particularly aims at exploring and discovering how those synthetic intrusions and their associated orientations can be recovered and interpreted from 3D inversions. The 3D synthetic data were generated using the 3D forward code in WinGLink of Mackie et al. (1994). Furthermore, 2.5% random noise was added to the numerically calculated impedances of the 19 stations per profile.

As for the real MT data, the 3D inversion code WSINV3DMT (Siripunvaraporn et al., 2005a) was used to invert the full impedance tensors from each data set A and B. In total, four 3D inversion models are presented here. Each synthetic data set generated from models A and B were inverted using two different *a priori* models: (1) a simple half-space of 100 Ω m and (2) a 2D model closer to the original 3D inversion models, with the aim of obtaining a more constrained inversion. The resulting inversion models are identified as A1, A2, B1 and B2 (Fig. 5). In all cases, the starting model

used in the inversions was a uniform half-space of 100 Ω m. Similar to the real data inversion, here an error floor of 2.5% of the magnitude of the geometrically-averaged off-diagonal impedances was used to set a minimum error bar to $0.025 * (Zxy * Zyx)^2$ applied on all four elements of the impedance tensor during the inversion. Note that this is half the error floor defined for the real MT impedance data (above).

First of all, both unconstrained models A1 and A2 show final overall RMS misfits of 1.8. South of the profile the resistivity structure of the original models is fairly well recovered, although the top of the conductive layer is seen at slightly shallower depths. However, further north, where the environment becomes more 3D, the lateral resolution of the intrusive structures becomes poorer as the mid-crustal conductor dips steeply to the north. It is clear that for each model A1 and B1, the data detect conductive structures due to the intrusions north of the profile. However, with the poor lateral coverage related to the "one profile" configuration of the stations, the conductive anomaly deepens to the north along the profile.

In order to compensate for the lack of lateral coverage, a second inversion scheme was applied. Models A2 and B2 were obtained by introducing a new simple 2D *a priori* model closer to the original 3D synthetic models. This *a priori* model was based particularly on the assumption of a horizontal conductive intrusion to the north into a more resistive block (Fig. 5). For both inversions A2 and B2 the final overall RMS misfit was reduced to 1.1 after following an identical inversion parameterization as for models A1 and B1. Thus, the use of an *a priori* model has allowed the inversion to avoid the local minimum associated with models A1 and B1 and to discover superior models that fit almost a factor of 2 better. It is worth noting that the use of the new *a priori* model decreases also the individual RMS misfits for all sites (Fig. 5). The main difference in the new A2 and B2 models is the substantial improvement of the lateral resolution for the 3D intrusions located beneath the northern part of the profile. Although, each intrusion obviously
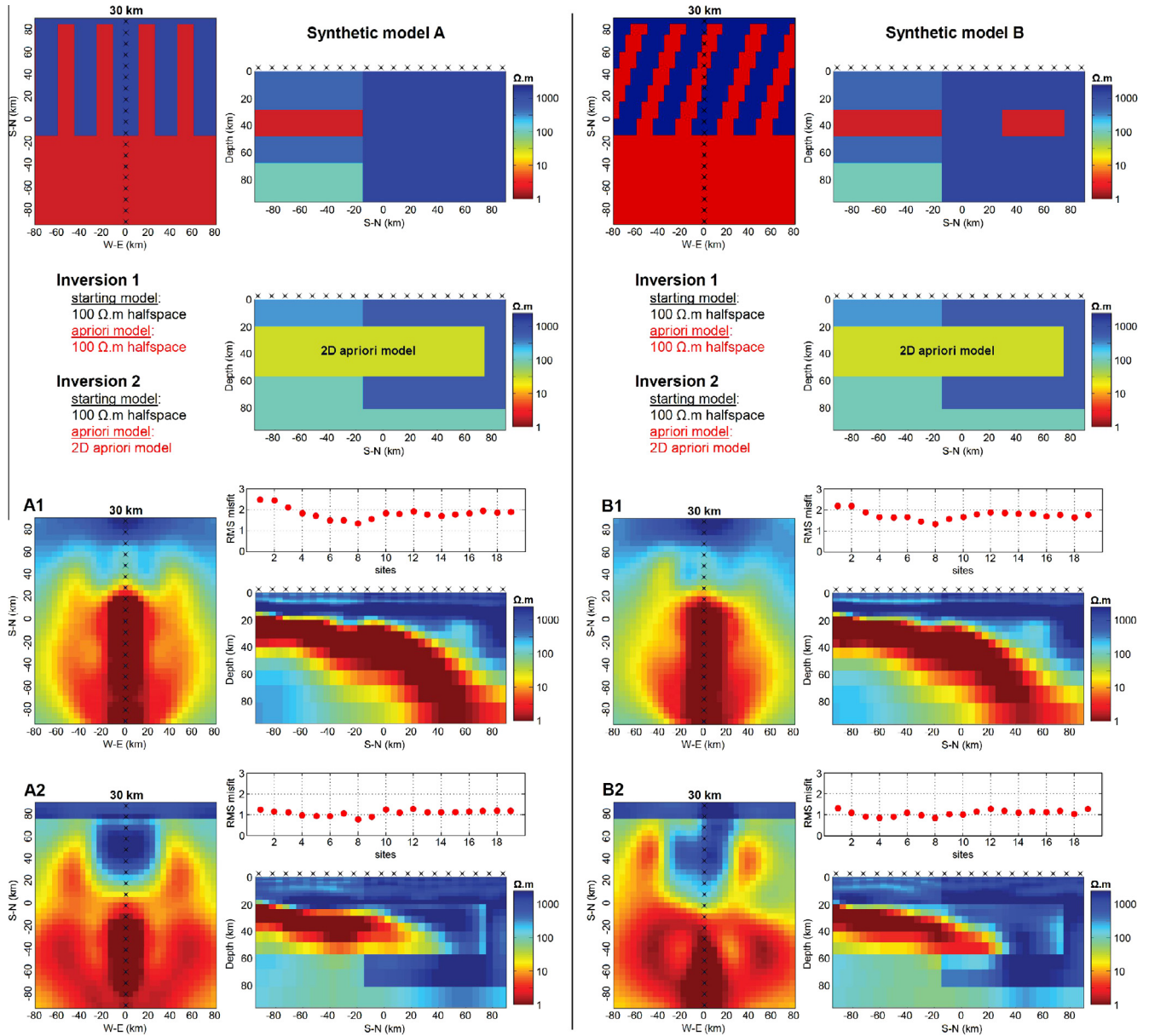
Fig. 5. 3D synthetic study – The 3D synthetic models consist on a 1500 Ω m resistive and 150 km thick block to the north. The southern block is 500 Ω m resistive and 70 km thick with an embedded 2 Ω m conductive layer between 30 and 50 km. The later turns into 3D intrusions in the more resistive block: the only difference between models A and B. Both blocks are underlain by a 100 Ω m half-space. The inversion results for inversions A1, A2, B1 and B2 are presented with a plane view at 30 km as well as north–south cross-sections right beneath the stations. The RMS misfit is plotted for each site for each inversion. For inversion 2, the *a priori* model is mainly defined by relatively thicker 30 Ω m mid-lower crustal layer embedded into a thinner 600 Ω m resistive block to the north and overlain by a 300 Ω m layer to the south.

cannot be defined clearly due to the 15 km width and depth of each anomaly, this second set of inversions appears to be more sensitive to lateral structures. Even the preferential orientation of the original intrusion can be recovered, as seen on model B2 where the resistive and conductive anomalies are slightly orientated towards the east in the northern part of the profile (Fig. 5). By forcing the embedding of the conductive layer in the more resistive block, the conductive anomaly located previously deeper beneath the profile is now relocated on each side of the profile, giving more support to the original 3D models by improving lateral resolution somewhat.

Finally, in the northern part of the profile, the inversion can still sense the resistor extending further with depth as in the original model, highlighting the propagation of the sensitivity

of the data beyond the constraints of the *a priori* model. However, due to the sharp layer transition generated by the *a priori* model, inversions could be inhibited and therefore must be viewed with caution. Fig. 6 shows the observed synthetic data generated from models A and B as well as the calculated MT data from models A1, A2, B1 and B2. The main difference between the model A and B can be clearly seen on the XX and YY components of the apparent resistivity. For model A, the diagonal elements of the impedance tensor are quite low at all sites and periods. Furthermore, although the effect of the introduction of the *a priori* model is not obvious on the responses associated with model A, model B shows a net improvement for the responses of the diagonal elements, particularly for apparent resistivity.
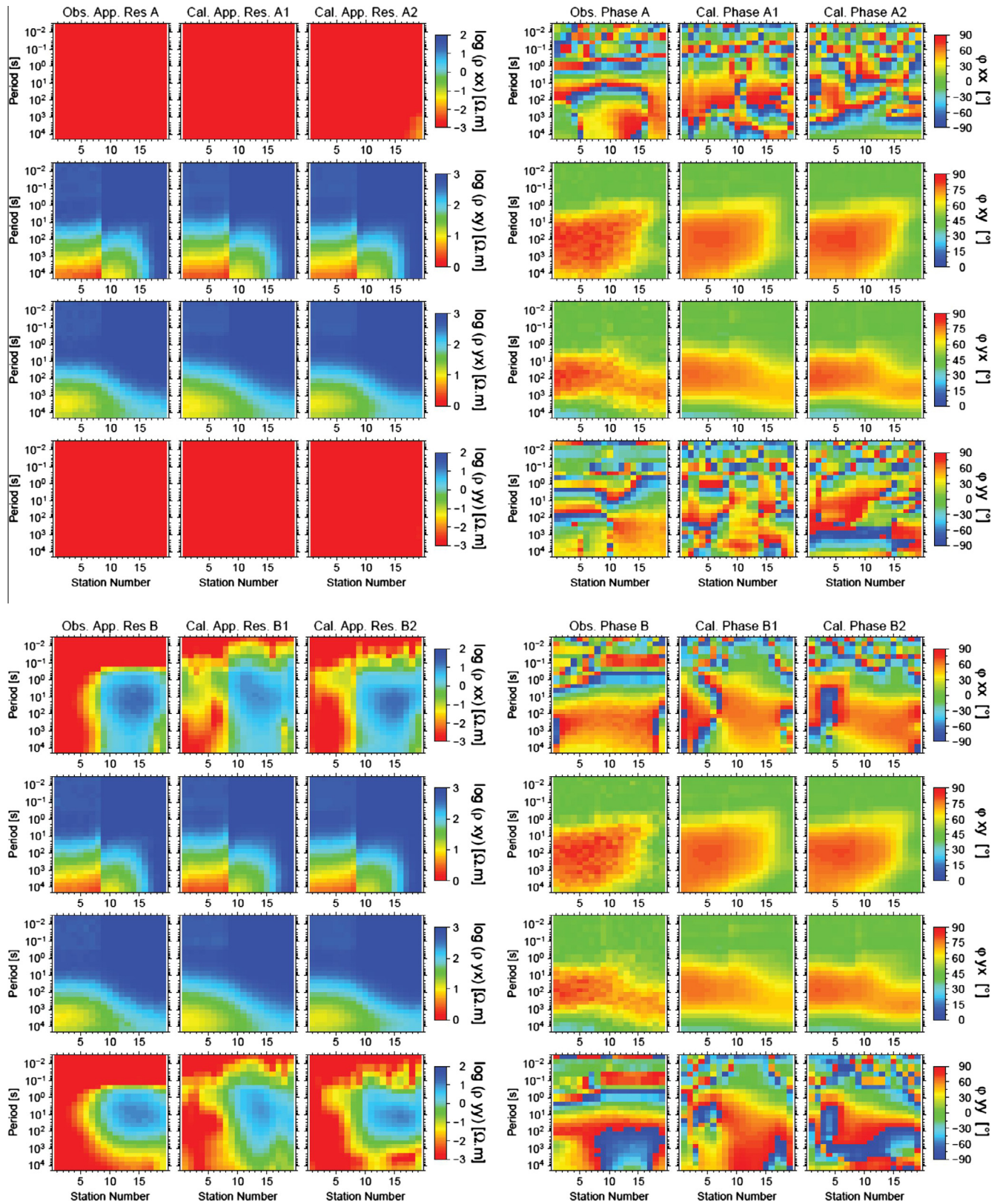
Fig. 6. Observed synthetic data generated from models A and B associated with calculated data from the inversion models A1, A2, B1 and B2. The station numbers increases to the north. The data is plotted as pseudo-sections of apparent resistivity and phase for all 4 components of the impedance tensor.
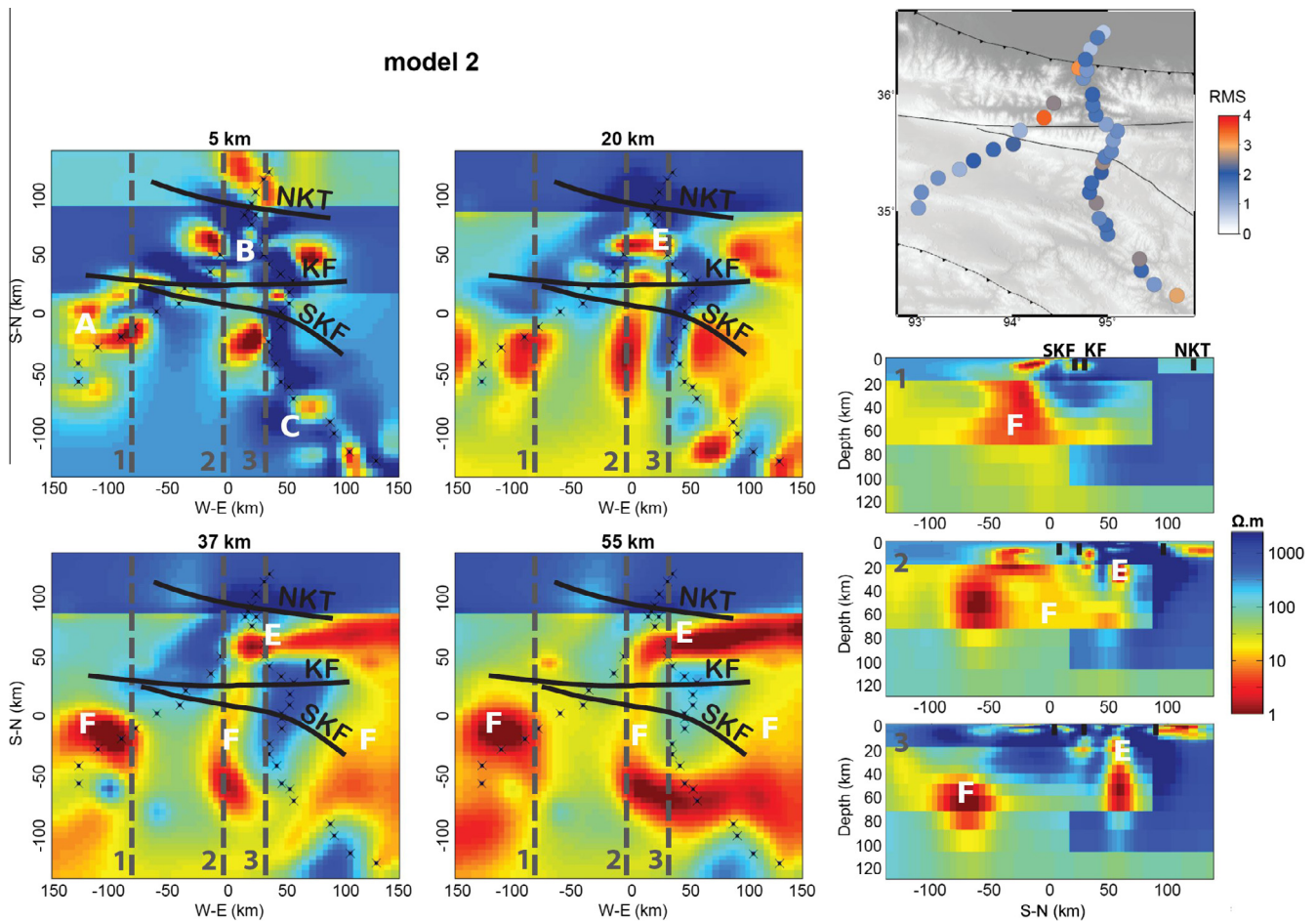
Fig. 7. 3D model 2 of the INDEPTH data obtained from the inversion of the full impedance tensor and constrained by a 2D *a priori* model. The 3D model is plotted for several horizontal slices at different depths and for cross-sections with locations shown on plane views. The RMS misfit of the inversion is shown for each site on the top right corner. KF, Kunlun fault; SKF, South Kunlun fault; NKT, North Kunlun thrust.

4.3. Constrained 3D inversion of the INDEPTH data

Following the results of the synthetic study above, a second 3D inversion of the INDEPTH data is presented here, where this time the inversion is controlled by the use of a 2D *a priori* model. This *a priori* model was based on the previous MT studies in the area (Unsworth et al., 2004; Le Pape et al., 2012) and is therefore very similar to the 2D *a priori* model used in the above synthetic study. This new 3D inversion followed a similar scheme to the first unconstrained model 1 presented above (Fig. 3), with the only difference being the introduction of a different *a priori* model. As seen on Fig. 7, the inversion is controlled by a 2D model defined by a 30 Ω m layer located between 20 and 70 km based on the assumption of whole crustal partial melting. This layer is embedded in the more resistive block characterizing the Kunlun–Qaidam terrane to the north. The latter is 600 Ω m resistive and limited to 100 km thickness extent in order to avoid too much of a resistive constraint on the model. To the south, a 300 Ω m layer describes the upper crust of the Songpan–Ganzi terrane. Furthermore, the Qaidam basin was modelled by a 100 Ω m 12 km thick layer to avoid the smearing of the highly conductive structure characterizing the basin. The *a priori* model resistivities were chosen relatively close to each other to limit significant lateral and vertical resistivity contrasts that could lead to the generation of over-fitting artefacts in the model. Furthermore, the transition between the two main blocks was located beneath the surficial trace of the Kunlun fault.

The results of the inversion (Fig. 7) are interesting as they show an improvement in fit to the data at some stations located north of the Kunlun fault and contribute to an overall RMS misfit of 1.9. The observed and calculated MT data obtained from model 2 are plotted on Fig. 8. Furthermore, comparison of both observed and calculated curves of apparent resistivity and phase for all 4 components can be found in the Supplementary information. The new restrictions applied to the inversion through the use of 2D *a priori* model mainly enabled a limiting in the downward leakage of some of the conductive artefacts observed in model 1 (Fig. 3). In a similar manner to that demonstrated in the synthetic MT study, this new model also improved the lateral resolution around the profiles. The plan view at 5 km depth presents once again interesting correlations with the surficial traces of the major tectonic features beyond the lateral boundaries created by the *a priori* model. To the west, the SKF and KF describe the limit of the conductive sediments denoted by feature "A" of the Songpan–Ganzi terrane. To the east, the upper crustal resistive structures "C" can be related again to the Bayan Har mountains. The main resistive features "B" observed on the model located north of the Kunlun fault likely define extruded Proterozoic basement and plutonic intrusions characteristic of the Kunlun Shan (Cowgill et al., 2003). The resistive structure located just south of the NKT at a depth shallower than 30 km is likely to be part of the Kunlun Batholith, a significant feature of the north Kunlun ranges (Yin and Harrison, 2000).

The extension of all different structures with depth can be seen on the cross-sections 2 and 3 (Fig. 7). The horizontal slices at 20 km
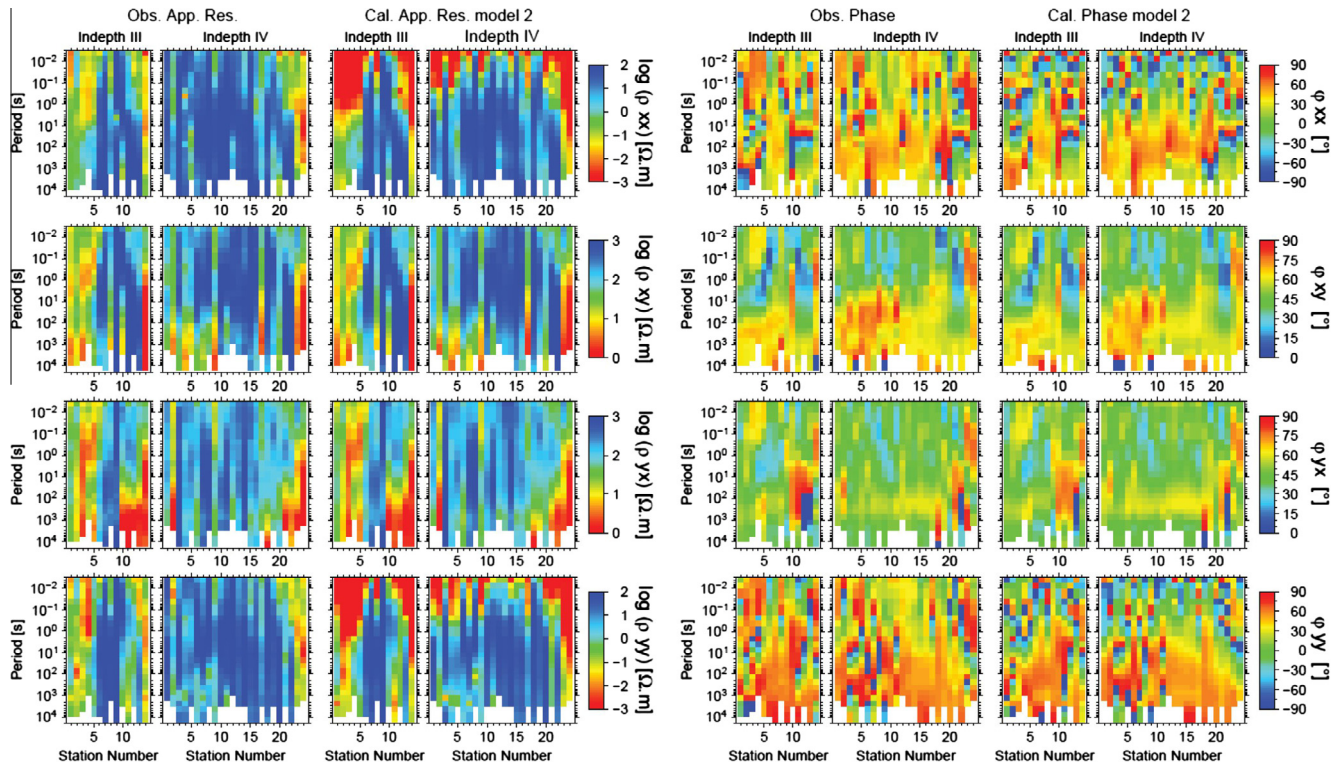
Fig. 8. Observed and calculated data from the inversion model 2. The data is separated as INDEPTH III and IV sections. For each section, the station numbers increase to the north. The data is plotted as pseudo-sections of apparent resistivity and phase for all 4 components of the impedance tensor.

and 37 km particularly show strong north–south aligned lateral changes in the resistivity structures. Those alternations, more clearly seen in model 2 than in model 1, cross the Kunlun fault to the north. Indeed, beneath the Kunlun fault system, the INDEPTH IV profile defines a resistive feature surrounded by conductive material "F" on each of its sides. The synthetic inversion study (Fig. 5) also confirms the fact that at middle-to-lower crust depths the lateral resolution on structures at least 50 km outside the profiles is reasonably accurate. Furthermore, as seen on model 1 another conductive anomaly "E" is located between the KF and NKT, and seems to be superposed to the anomaly intrusion from the south. This second conductive anomaly beneath the Kunlun Shan could be linked to crustal fluids released from the southeast-dipping North Kunlun thrust. Cross-section 2 when compared to model 1 particularly highlights now the clear intrusion of the conductive middle to lower crust "F" of the Songpan–Ganzi terrane to the north across the Kunlun fault. As mentioned previously, cross-section 1 is not well constrained and little can be concluded from it, but the aim here is to see how the introduction of the resistive block removed the leakage of the conductivity anomaly observed on the cross-section 1 of the model 1.

5. Discussion and interpretation

Although based on two MT profiles, and therefore characterized by resolution issues associated with the paucity of spatial coverage, the 3D inversion models reveal interesting features and show once again that the resistivity structure of this part of the Tibetan plateau is spatially quite complex. The synthetic modelling demonstrates that lateral resolution can be improved with the introduction of a trusted *a priori* model. However, in order to constrain the full 3D structure, additional MT profiles or a grid of MT stations are required to increase sensitivity and resolution, both laterally and in depth (Siripunvaraporn et al., 2005b). In comparison to model 1, some clear improvement in the lateral resolution of the

3D structures can be seen in model 2. However, one comforting aspect in having the models 1 and 2 is the consistency and reliability of some structures that are common features for both models. Those are less likely to be artefacts of the inversion. Furthermore, as the *a priori* model is an approximation, it may also control structures that are too confining, and therefore the observations from the model 1 should not be neglected in the interpretation.

Several interesting features can be seen in both models 1 and 2 and it is also worth noting that the main observed conductive structures are quite in agreement with the inductions arrows plotted on Fig. 2. To the north, the geometry of the southern part of the conductive Qaidam basin is well recovered spatially by the MT data and is quite well constrained in the model 2. Furthermore, the high resistivity of the Kunlun–Qaidam block, associated with its colder thermal conditions compared to the Songpan–Ganzi block, is also a consistent feature from both inversions and extends to depths of around 130 km, as seen on model 1. The later observation is in agreement with the tomographic results from Ceylan et al. (2012). However, due to the lack of stations, which inhibits resolution of mantle structures in the model, it is difficult to exclude the model of Asian lithosphere subduction (Zhao et al., 2011).

Both models show also a conductive anomaly elongated along and located south of the surficial trace of the North Kunlun thrust. This anomaly is elongated in an east–west direction and propagates to the east with depth. One interpretation would be the presence of fluids associated with the south-east dipping North Kunlun thrust. To the south, both models 1 and 2 exhibit a widespread middle to lower crust conductive anomaly extending to the South Kunlun fault. Due to the presence of strong crustal conductors and also the lack of lateral coverage, the resolution to the mantle structures of the Songpan–Ganzi terrane is challenging. As discussed by Li et al. (2003), it is possible that metallic minerals and graphite exists locally in Tibet. However, since the main crustal anomaly beneath the Qiangtang and Songpan–Ganzi terranes crosses major terrane boundaries as it extends further south in the Lhasa terrane

(Wei et al., 2001), graphite and metallic minerals are likely not responsible for the observed large spatial extend of the crustal conductive anomaly. Furthermore, Yoshino and Noritake (2011) have shown that graphite is not stable at the temperatures expected to characterize the middle-to-lower Tibetan crust, i.e., temperatures in excess of 700 °C.

The main crustal anomaly observed on the resistivity models has been interpreted to be related to widespread partial melting of the middle-to-lower crust (Unsworth et al., 2004; Le Pape et al., 2012). The partial melting of the crust under anomalously high temperatures (Owens and Zandt, 1997; Mechie et al., 2004) is in agreement with the presence of thin Tibetan lithosphere beneath northern Tibet (McNamara et al., 1997; Zhao et al., 2011; Agius and Lebedev, 2013). The latter feature may enhance the heat flow in a crust already exceptionally thick enough to produce high radiogenic heat generation. Furthermore, the presence of partially molten crust is also in agreement with the presence of Miocene to Quaternary felsic magmas in the southern Kunlun Shan, just north of the Kunlun fault. Those felsic magmas have been interpreted to originate from crustal melts (Wang et al., 2012). Both models 1 and 2 show the intrusion of Songpan–Ganzi conductive material to the north beyond the Kunlun fault. Based on the assumption that most of the conductive anomaly is associated with crustal melt, the constrained 3D model 2 presents superior resolution of the Songpan–Ganzi partially molten crust melt intrusion to the north into the more resistive Kunlun–Qaidam block. Finally, it can be noted that the evolution of the crustal conductive anomaly from south to north is quite in agreement with the changes in the induction vectors orientations (Fig. 2). South of the SKS, the vectors pointing to the south are quite strong and are associated with a homogeneous conductive anomaly. North of the SKS, they become weaker and west-orientated reflecting the lateral changes characterizing the conductive intrusions observed in the 3D model.

These observations are very consistent with the results of 2D anisotropic modelling of the 600-line (Le Pape et al., 2012). However, although the prior 2D anisotropic study of Le Pape et al. (2012) mainly revealed the extension of the partial melt from the Songpan–Ganzi crust further north in a finger-like manner of intrusion, the results drawn from the modelling did not bring further constraints on the geometry of the observed anomaly. The new models and results associated with the introduction of the new INDEPTH IV MT data bring a superior understanding on the distribution of those intrusions. The 3D model 2 particularly highlights not only one but two north–south orientated intrusive channels located on each side of the INDEPTH IV profile. Despite resolution issues at the depth of the anomaly, the electrical anisotropy previously observed in the area appears to be more likely related to macroscopic anisotropy associated with a heterogeneous extension of the partial molten Songpan–Ganzi crust to the north. The locations of the two INDEPTH profiles particularly enable us to constrain an upper limit on the width of one of the channels. Indeed, the conductive anomaly located between the two profiles and extending across the Kunlun fault appears to be 40–50 km wide as it is surrounded by trusted and well resolved lateral resistive features.

Despite a better understanding in the geometry of the intrusive anomaly, as seen on the synthetic modelling (Fig. 5), the 3D inversion of the profile data struggles to recover the true resistivity of the original anomaly, particularly for structures off-profile. Therefore, at this stage only approximate estimates of the fraction of melts have been considered. The more conductive anomaly "E" (Fig. 7) located just south of the NKT was not taken into account as probably it is involving crustal fluids released from the NKT. Based on the 3D model 2, the Songpan–Ganzi crust high conductivity anomaly is mainly ranging between 3 and 10 Ω m in resistivity,

whereas for the Kunlun crust the resistivity of the anomaly ranges from 6 to 30 Ω m. Using the Partzsch et al. (2000) modified brick layer model, the fraction of melt beneath the Songpan–Ganzi terrane is expected to be between 4% and 15%, in agreement with previous studies (Bai et al., 2010; Rippe and Unsworth, 2010), whereas for the Kunlun crust the intrusive channels would have lower fractions of melt ranging from 2% to 8%. Following the arguments of Rippe and Unsworth (2010), it is concluded that the decrease of melt fraction to the north implies a reduction of viscosity and therefore a decrease in the velocity of flow along the channels. Furthermore, with a limited signature of channel flow at the surface, the separated intrusive channels of the Songpan–Ganzi crust are probably flowing in a similar manner as the "tunnel flow model" presented by Beaumont et al. (2001). Finally, the overall viscosity of the Kunlun crust would still be in agreement with a significant drop in viscosity as observed by Ryder et al. (2011), reflecting the lateral changes in the rheology of the Kunlun crust emphasised by the 3D resistivity modelling.

Acknowledgements

Appendix A. Supplementary data

Supplementary data associated with this article can be found, in the online version, at http://dx.doi.org/10.1016/j.pepi.2014.07.004.

References

Agius, M.R., Lebedev, S., 2013. Tibetan and Indian lithospheres in the upper mantle beneath Tibet: evidence from broadband surface-wave dispersion. Geochem. Geophys. Geosyst. 14, 4260–4281.

Bai, D., Unsworth, M.J., Meju, M.A., Ma, X., Teng, J., Kong, X., Sun, Y., Sun, J., Wang, L., Jiang, C., Zhao, C., Xiao, P., Liu, M., 2010. Crustal deformation of the eastern Tibetan plateau revealed by magnetotelluric imaging. Nat. Geosci. 3, 358–362.

Beaumont, C., Jamieson, R.A., Nguyen, M.H., Lee, B., 2001. Himalayan tectonics explained by extrusion of a low-viscosity channel coupled to focused surface denudation. Nature 414, 738–742.

Burchfiel, B.C., Chen, Z., Liu, Y., Royden, L.H., 1995. Tectonics of the Longmen Shan and adjacent regions, central China. Int. Geol. Rev. 37, 661–735.

Caldwell, T.G., Bibby, H.M., Brown, C., 2004. The magnetotelluric phase tensor. Geophys. J. Int. 158, 457–469.

Ceylan, S., Ni, J., Chen, J.Y., Zhang, Q., Tilmann, F., Sandvol, E., 2012. Fragmented indian plate and vertically coherent deformation beneath eastern Tibet. J. Geophys. Res. 117, B11303.

Chen, L.H., Booker, J.R., Jones, A.G., Wu, N., Unsworth, M.J., Wei, W.B., Tan, H.D., 1996. Electrically conductive crust in southern Tibet from INDEPTH magnetotelluric surveying. Science 274, 1694–1696.

Clark, M.K., Royden, L.H., 2000. Topographic ooze: building the eastern margin of Tibet by lower crustal flow. Geology 28, 703–706.

Cowgill, E., Yin, A., Harrison, T.M., Xiao-Feng, W., 2003. Reconstruction of the Altyn Tagh fault based on U-Pb geochronology: role of back thrusts, mantle sutures, and heterogeneous crustal strength in forming the Tibetan Plateau. J. Geophys. Res. 108 (B7), 2346.

Egbert, G.D., 1997. Robust multiple-station magnetotelluric data processing. Geophys. J. Int. 130, 475–496.

Gehrels, G.E., Kapp, P., DeCelles, P., Pullen, A., Blakey, R., Weislogel, A., Ding, L., Guynn, J., Martin, A., McQuarrie, N., Yin, A., 2011. Detrital zircon geochronology of pre-Tertiary strata in the Tibetan-Himalayan orogen. Tectonics 30, TC5016.

Godin, D., Grujic, D., Law, R.D., Searle, M.P., 2006. Channel flow, ductile extrusion and exhumation in continental collision zones. In: Law, R.D., Searle, M.P., Godin, L. (Eds.), Channel Flow, Ductile Extrusion and Exhumation in Continental Collision Zones: An Introduction, vol. 268. Geological Society, London, Special Publications, pp. 1–23 (Chap.).

Haines, S.S., Klemperer, S.L., Brown, L., Jingru, G., Mechie, J., Meissner, R., Ross, A., Wenjin, Z., 2003. INDEPTH III seismic data: from surface observations to deep crustal processes in Tibet. Tectonics 22.

Harris, N., 2007. Channel flow and the Himalayan-Tibetan orogen: a critical review. J. Geol. Soc. 164 (3), 511–523.

Huang, C.K., Ye, T.Z., Chen, K.Q., Wu, K.L., Ji, X.Y., Gao, Z.J., Qian, D.D., Tian, Y.Y., He, Y.X., Zhan, Q.H., Cao, B.G., Li, L., Shao, H.M., Wang, Y.Q., Yang, M.G., Zhang, Z.W., Yao, D.S., Zheng, J.K., 2004. Geological Map of the People's Republic of China. SinoMaps Press, Xian.

Jones, A.G., 1986. Parkinson's pointers' potential perfidy! Geophys. J. R. Astron. Soc. 87, 1215–1224.

Jones, A.G., 2012. Distortion of magnetotelluric data: its identification and removal. In: Chave, A.D., Jones, A.G. (Eds.), The Magnetotelluric Method: Theory and Practice. Cambridge, UK: Cambridge University Press (Chapter 6).

Jones, A.G., Jödicke, H., 1984. Magnetotelluric transfer function estimation improvement by a coherence-based rejection technique. In: 54th Ann. Mtg. Soc. of Expl. Geophys., Atlanta, Georgia.

Jones, A.G., Chave, A.D., Egbert, G.D., Auld, D., Bahr, K., 1989. A comparison of techniques for magnetotelluric response function estimates. J. Geophys. Res. 94, 14,201–14,213.

Karplus, M.S., Zhao, W., Klemperer, S.L., Wu, Z., Mechie, J., Shi, D., Brown, L.D., Chen, C., 2011. Injection of Tibetan crust beneath the south Qaidam Basin: evidence from INDEPTH IV wide-angle seismic data. J. Geophys. Res. 116.

Karplus, M.S., Klemperer, S.L., Lawrence, J.F., Zhao, W., Mechie, J., Tilmann, F., Sandvol, E., Ni, J., 2013. Ambient-noise tomography of north Tibet limits geological terrane signature to upper-middle crust. Geophys. Res. Lett. 40, 808–813.

Kezao, C., Bowler, J.M., 1986. Late pleistocene evolution of salt lakes in the Qaidam basin, Qinghai province, China. Palaeogeogr. Palaeoclimatol. Palaeoecol. 54.

Kirby, E., Harkins, N., Wang, E., Shi, X., Fan, C., Burbank, D., 2007. Slip rate gradients along the eastern Kunlun fault. Tectonics 26.

Kiyan, D., Jones, A.G., Vozar, J., 2013. The inability of magnetotelluric off-diagonal impedance tensor elements to sense oblique conductors in three-dimensional inversion. Geophys. J. Int. 196, 1351–1364.

Klemperer, S., 2006. Channel flow, ductile extrusion and exhumation in continental collision zones. In: Law, R.D., Searle, M.P., Godin, L. (Eds.), Crustal Flow in Tibet: Geophysical Evidence for the Physical State of Tibetan Lithosphere, and Inferred Patterns of Active Flow, Vol. 268. Geological Society, London, Special Publications, pp. 39–70 (Chapter).

Le Pape, F., Jones, A.G., Vozar, J., Wenbo, W., 2012. Penetration of crustal melt beyond the Kunlun fault into northern Tibet. Nat. Geosci. 5, 330–335.

Li, S., Unsworth, M.J., Booker, J.R., Wei, W., Tan, H., Jones, A.G., 2003. Partial melt or aqueous fluids in the Tibetan crust: constraints from INDEPTH magnetotelluric data. Geophys. J. Int. 153, 289–304.

Mackie, R.L., Smith, J.T., Madden, T.R., 1994. Three-dimensional electro-magnetic modeling using finite difference equations: the magnetotelluric example. Radio Sci. 29, 923–935.

McNamara, D.E., Walter, W.R., Owens, T.J., Ammon, C.J., 1997. Upper mantle velocity structure beneath the Tibetan Plateau from Pn travel time tomography. J. Geophys. Res. 102 (B1), 493–505.

Mechie, J., Sobolev, S.V., Ratschbacher, L., Babeyko, A.Y., Bock, G., Jones, A.G., Nelson, K.D., Solon, K.D., Brown, L.D., Zhao, W., 2004. Precise temperature estimation in the tibetan crust from seismic detection of the α-β quartz transition. Geology 32, 601–604.

Mechie, J., Zhao, W., Karplus, M.S., Wu, Z., Meissner, R., Shi, D., Kemplerer, S.L., Su, H., Kind, R., Xue, G., Brown, L.D., 2012. Crustal shear velocity and Poisson's ratio structure along the INDEPTH IV profile in northeast Tibet as derived from wide-angle seismic data. Geophys. J. Int. 191, 369–384.

Medvedev, S., Beaumont, C., 2006. Channel flow, ductile extrusion and exhumation in continental collision zones. In: Law, R.D., Searle, M.P., Godin, L. (Eds.).Growth of Continental Plateaus by Channel Injection: Models Designed to Address Constraints and Thermomechanical Consistency, Vol. 268. Geological Society, London, Special Publications, pp. 147–164 (Chapter).

Meyer, B., Tapponnier, P., Bourjot, L., Metivier, F., Gaudemer, Y., Peltzer, G., Shunmin, G., Zhitai, C., 1998. Crustal thickening in Gansu Qinghai, lithospheric mantle subduction, and oblique, strike slip controlled growth of the Tibet plateau. Geophys. J. Int. 135 (1), 1–47.

Nelson, K.D., Zhao, W., Brown, L.D., Kuo, J., Che, J., Liu, X., Klemperer, S.L., Makovsky, Y., Meissner, R., Mechie, J., Kind, R., Wenzel, F., Ni, J., Nabelek, J., Chen, L., Tan, H., Wei, W., Jones, A.G., Booker, J., Unsworth, M., Kidd, W.S.F., Hauck, M., Alsdorf, D., Ross, A., Cogan, M., Wu, C., Sandvol, E., Edwards, M., 1996. Partially molten middle crust beneath southern Tibet: synthesis of Project INDEPTH results. Science 274, 1684–1686.

Owens, T.J., Zandt, G., 1997. Implications of crustal property variations for models of Tibetan plateau evolution. Nature 387, 37–43.

Parkinson, W.D., 1959. Directions of rapid geomagnetic fluctuations. Geo-phys. J. R. Astron. Soc. 2 (1), 1–14.

Partzsch, G.M., Schilling, F.R., Arndt, J., 2000. The influence of partial melting on the electrical behavior of crustal rocks: laboratory examinations, model calculations and geological interpretations. Tectonophysics 317, 189–203.

Rippe, D., Unsworth, M., 2010. Quantifying crustal flow in Tibet with magnetotelluric data. Phys. Earth Planet. Inter. 179, 107–121.

Rousseeuw, P.J., 1984. Least median of squares regression. J. Am. Stat. Assoc. 79, 871–880.

Royden, L.H., Burchfiel, B.C., King, R.W., Wang, E., Chen, Z., Shen, F., Liu, Y., 1997. Surface deformation and lower crustal flow in eastern Tibet. Science 276, 788–790.

Ryder, I., Bürgmann, R., Pollitz, F., 2011. Lower crustal relaxation beneath the Tibetan Plateau and Qaidam Basin following the 2001 Kokoxili earthquake. Geophys. J. Int. 187, 613–630.

Searle, M.P., Elliott, J.R., Phillips, R.J., Chung, S.L., 2011. Crustal-lithospheric structure and continental extrusion of Tibet. J. Geol. Soc. London 168, 633–672.

Siripunvaraporn, W., Egbert, G., Lenbury, Y., Uyeshima, M., 2005a. Three-dimensional magnetotelluric inversion: data-space method. Phys. Earth Planet. Inter. 150, 3–14.

Siripunvaraporn, W., Egbert, G., Uyeshima, M., 2005b. Interpretation of two-dimensional magnetotelluric profile data with three-dimensional inversion: synthetic examples. Geophys. J. Int. 160, 804–814.

Smirnov, M.Y., 2003. Magnetotelluric data processing with a robust statistical procedure having a high breakdown point. Geophys. J. Int. 152, 1–7.

Tapponnier, P., Xu Zhiqin, X., Roger, F., Meyer, B., Arnaud, N., Wittlinger, G., Jingsui, Y., 2001. Oblique stepwise rise and growth of the Tibet Plateau. Science 294, 1671–1677.

Unsworth, M., Wei, W., Jones, A.G., Li, S., Bedrosian, P., Booker, J., Jin, S., Deng, M., Tan, H., 2004. Crustal and upper mantle structure of northern Tibet imaged with magnetotelluric data. J. Geophys. Res. 109, B02403.

Wang, Q., Chung, S.L., Li, X.H., Wyman, D., Li, Z.X., Sun, W.D., Qiu, H.N., Liu, Y.S., Zhu, Y.T., 2012. Crustal melting and flow beneath northern Tibet: evidence from mid-Miocene to quaternary strongly Peraluminous Rhyolites in the southern Kunlun range. J. Petrol. 53 (12), 2523–2566.

Wei, W., Unsworth, M., Jones, A.G., Booker, J., Tan, H., Nelson, D., Chen, L., Li, S., Solon, K., Bedrosian, P., Jin, S., Deng, M., Ledo, J., Kay, D., Roberts, B., 2001. Detection of widespread fluids in the Tibetan crust by magnetotelluric studies. Science 292, 716–718.

Yao, H.J., Beghein, C., Van Der Hilst, R.D., 2008. Surface wave array tomography in SE Tibet from ambient seismic noise and two-station analysis-II. Crustal and upper-mantle structure. Geophys. J. Int. 173, 205–219.

Yin, A., Harrison, T.M., 2000. Geologic evolution of the Himalayan-Tibetan orogen. Annu. Rev. Earth Planet. Sci. 28 (1), 211–280.

Yin, A., Nie, S., 1996. A phanerozoic palinspastic reconstruction of China and its neighboring regions. In: Yin, A., Harrison, T.M. (Eds.), The Tectonics of Asia. New York: Cambridge Univ. Press, pp. 442–485.

Yin, A., Chen, X., McRivette, M.W., Wang, L., Jiang, W., 2008. Cenozoic tectonic evolution of Qaidam basin and its surrounding regions (Part 1): the north Qaidam thrust system. Geol. Soc. Am. Bull. 120, 813–846.

Yoshino, T., Noritake, F., 2011. Unstable graphite films on grain boundaries in crustal rocks. Earth Planet. Sci. Lett. 306, 186–192.

Zhao, W., Kumar, P., Mechie, J., Kind, R., Meissner, R., Wu, Z., Shi, D., Su, H., Xue, G., Karplus, M., Tilmann, F., 2011. Tibetan plate overriding the Asian plate in central and northern Tibet. Nat. Geosci. 4, 870–873.